

# Steering from electrochemical denitrification to ammonia synthesis

Received: 15 September 2022

Accepted: 3 January 2023

Published online: 07 January 2023

Check for updates

Huan Li<sup>1,2</sup>, Jun Long<sup>1</sup>, Huijuan Jing<sup>1,2</sup> & Jianping Xiao<sup>1,2</sup>

The removal of nitric oxide is an important environmental issue, as well as a necessary prerequisite for achieving high efficiency of CO<sub>2</sub> electroreduction. To this end, the electrocatalytic denitrification is a sustainable route. Herein, we employ reaction phase diagram to analyze the evolution of reaction mechanisms over varying catalysts and study the potential/pH effects over Pd and Cu. We find the low N<sub>2</sub> selectivity compared to N<sub>2</sub>O production, consistent with a set of experiments, is limited fundamentally by two factors. The N<sub>2</sub>OH\* binding is relatively weak over transition metals, resulting in the low rate of as-produced N<sub>2</sub>O\* protonation. The strong correlation of OH\* and O\* binding energies limits the route of N<sub>2</sub>O\* dissociation. Although the experimental conditions of varying potential, pH and NO pressures can tune the selectivity slightly, which are insufficient to promote N<sub>2</sub> selectivity beyond N<sub>2</sub>O and NH<sub>3</sub>. A possible solution is to design catalysts with exceptions to break the scaling characters of energies. Alternatively, we propose a reverse route with the target of decentralized ammonia synthesis.

Modern human activities, such as the excessive use of fertilizers, fossil-fuels combustion, and the discharge of industrial wastewater, have disrupted the ecological environment. As one of the major pollutants, nitrogen oxides (NO<sub>x</sub>) cause the damages of aquatic ecosystem, drinking water, photochemical smog, ozone depletion, and acid rain, posing threats to human health and the Earth's ecosystems<sup>1,2</sup>. Furthermore, carbon dioxide electroreduction (eCO<sub>2</sub>RR) is able to relieve global warming and is considered as an attractive route for sustainable production of fuels and chemicals<sup>3</sup>. However, it is usually unpractical to perform eCO<sub>2</sub>RR with a pure CO<sub>2</sub> feed. It was found a trace of nitric oxide (NO) (-0.8%) in feed greatly lower the efficiency by ~30%<sup>4</sup>. Therefore, the removal of nitrogen oxides has been recognized to be a necessary prerequisite for eCO<sub>2</sub>RR. Although the NO<sub>x</sub> can be thermochemically converted to N<sub>2</sub> by conventional denitrification technology, i.e. selective catalytic reduction (SCR)<sup>5</sup>. However, NO electroreduction reaction (eNORR)<sup>6–16</sup> should be a more compatible way with eCO<sub>2</sub>RR. Unfortunately, a high N<sub>2</sub> selectivity was not achieved experimentally over all studied catalysts, as illustrated in Fig. 1, compiled from the recent literatures<sup>17–19</sup>.

At -0.7 V vs. RHE, the observed N<sub>2</sub>O selectivity can be up to 95%, but with negligible N<sub>2</sub> production on Pd. As the electrode potential

drops to -0 V vs. RHE, the N<sub>2</sub>O selectivity is still higher compared to N<sub>2</sub> on Pd, Ag, Pt, Ni, Co, and Fe. In case the eNORR (on Pd and Ag) is performed in H-cell, the measured difference between N<sub>2</sub>O and N<sub>2</sub> selectivity can become smaller than that measured in flow-cell, while it does not overturn the dominance of N<sub>2</sub>O selectivity. Note that the pH effects in the range from 0.5 to 14 were also examined on Pd. Still, the N<sub>2</sub>O selectivity is higher with respect to the N<sub>2</sub> production. As the NO partial pressure (concentration) changes from 100 to 25%, the N<sub>2</sub> selectivity is still not desired compared to N<sub>2</sub>O production. If the electrode with higher overpotentials (<-0.3 V vs. RHE), it was demonstrated both N<sub>2</sub> and N<sub>2</sub>O will lose dominance, which will be overturned by NH<sub>3</sub> and H<sub>2</sub> productions. At low overpotential, the production of N<sub>2</sub>O is more favorable, while NH<sub>3</sub> or HER (hydrogen evolution reaction) are more selective at high overpotentials. In other words, the electrochemical denitrification with high N<sub>2</sub> selectivity was not achieved yet for both low and high overpotentials. Copper (Cu) is exceptional as shown in Fig. 1b and both N<sub>2</sub>O and N<sub>2</sub> are low in selectivity, which is even worse for the target of electrochemical denitrification.

In a word, all studied catalysts show higher selectivity to N<sub>2</sub>O than N<sub>2</sub> at low overpotentials (from 0.8 to -0.3 V vs. RHE). There must be some key factors in eNORR, which are extremely fundamental for all

<sup>1</sup>State Key Laboratory of Catalysis, Dalian Institute of Chemical Physics, Dalian National Laboratory for Clean Energy, Chinese Academy of Sciences, Dalian 116023, P. R. China. <sup>2</sup>University of Chinese Academy of Sciences, Beijing 100049, P. R. China. ✉e-mail: [xiao@dicp.ac.cn](mailto:xiao@dicp.ac.cn)

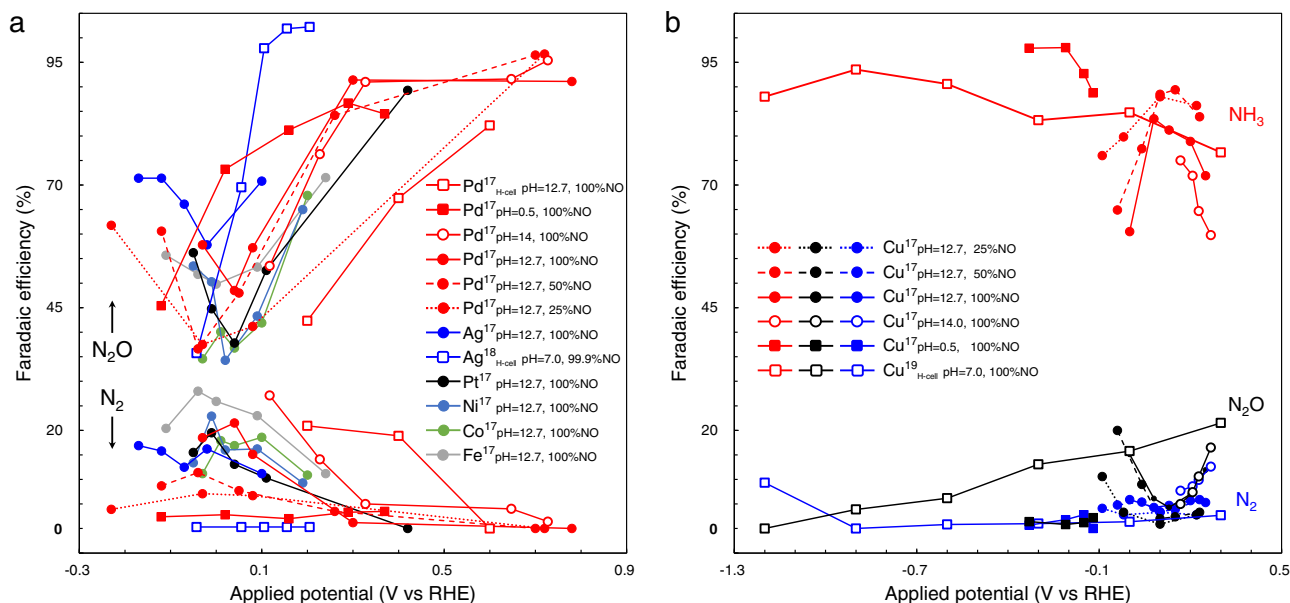


**Fig. 1 | Overview of different catalysts in eNORR compiled from the recent reports<sup>17–19</sup>.** **a** The Faradaic efficiency (FE) of N<sub>2</sub>O and N<sub>2</sub> at low overpotentials (0.8 to –0.3 V vs. RHE) on Pd, Ag, Pt, Ni, Co, and Fe. **b** A higher FE of NH<sub>3</sub> than dual-N products (N<sub>2</sub>O/N<sub>2</sub>) on Cu in a wider potential window (from 0.3 to –1.2 V vs. RHE).

studied transition metals (TMs) and determine the selectivity between N<sub>2</sub> and N<sub>2</sub>O. Are there any candidates from TM catalysts for effective electrochemical denitrification? If inexistent, why aren't TMs a great class of materials exhibiting high N<sub>2</sub> selectivity? What are the chemical origins of low N<sub>2</sub>-selectivity over all TMs? What nature of active sites (surface reactivity) can be the efficient catalysts for electrochemical denitrification? Understanding the fundamental limitations in selectivity over TMs can guide us in catalyst design of eNORR. Although the potential and pH effects slightly tune the selectivity, N<sub>2</sub> does never be the dominant product in diverse experimental conditions. We urgently need to understand the potential and pH effects on N<sub>2</sub> selectivity in eNORR too. The exceptional Cu primarily produce NH<sub>3</sub> rather than N<sub>2</sub>O and N<sub>2</sub> in the whole potential window for both H-cell and flow-cell. Why is Cu a special catalyst in eNORR? Are there any alternative and feasible choices of eNORR, e.g., to upgrade NO<sub>x</sub> to value-added chemicals (ammonia), rather than the conventional route of NO<sub>x</sub> removal?

These questions above are quite essential to discover new catalysts or developing novel route for eNORR. To these ends, we have performed density functional theory (DFT) calculations to establish the reaction phase diagram, which was used to study the evolution of reaction mechanism over TMs. Finally, we have also developed a microkinetic model to analyze the kinetics of exceptional eNORR on copper to answer the questions above.

## Results

### A general model for activity trend

To understand the higher N<sub>2</sub>O selectivity with respect to N<sub>2</sub> production, we need to study the mechanism of N-N bond formation and its evolution from most reactive catalysts (Fe) to medium ones (Co, Ni, Cu, Pt, and Pd), finally to the least reactive one (Ag). In general, there are two ways of N-N coupling for N<sub>2</sub> and N<sub>2</sub>O productions. The first one is that an adsorbed nitrogenous intermediates, such as N\*, NO\* and NOH\*, coupled with a NO molecule, namely Eley-Rideal-like (ER) mechanism<sup>8,20</sup>. The second one is the Langmuir-Hinshelwood (LH) mechanism<sup>20–22</sup> that is the combination of two adsorbed N-containing intermediates. The N-N coupling is a (thermo)chemical step without the direct involvement of proton and electron, which means that the energetics can be minimally affected by electrode potential. Therefore,

Most data points were measured in a flow-cell, while the open square symbols are detected values in a batch-type cell (H-cell). The data points for N<sub>2</sub>, N<sub>2</sub>O, and NH<sub>3</sub> from the same experimental conditions were connected, respectively.

we calculated the intrinsic barriers of nine possible ways of N-N coupling on multiple metals (Supplementary Figs. 1–6) to exclude some unlikely reaction pathways. For TMs (Fe, Ni, and Pd) with strong nitrogen binding, the ER mechanism (Supplementary Fig. 6a–c) are much more favorable than LH mechanism (Supplementary Fig. 6d–i). For TMs with weak reactivity, e.g., Cu and Ag, three ways (LH mechanism) were also excluded due to higher barriers (Supplementary Fig. 6g–i), namely, two N\* (or NOH\*) coupling and their cross-couplings. An exception is the comparable barriers of ER and LH mechanisms on Ag. Previously, we have found that the formation of N-N bond proceeds through two NO\* coupling on Ag<sup>23</sup>. Therefore, we only study the ER mechanisms and the two NO\* coupling (LH) mechanism in the following analysis. In addition, considering some primary protonation steps, totally 34 elementary reactions (Supplementary Table 1) were employed to enumerate all possible pathways for N<sub>2</sub> production.

To completely enumerate paths, all elementary steps were described with chemical vectors:

$$R_j = (\nu_{1j}, \nu_{2j}, \dots, \nu_{mj})^T \quad (1)$$

where  $\nu$  represents the stoichiometric number of the involved substances (reactants, intermediates, and products) in the relevant steps, and subscript  $m$  represents the index of substances in the reaction, subscript  $j$  represents the index of elementary steps. The total reaction network can be described by the following matrix  $S$ .

$$S = \begin{bmatrix} \nu_{11} & \cdots & \nu_{1n} \\ \vdots & \ddots & \vdots \\ \nu_{m1} & \cdots & \nu_{mn} \end{bmatrix} \quad (2)$$

where  $n$  refers to elementary steps in the reaction network. As a specific total reaction towards N<sub>2</sub>, N<sub>2</sub>O, NH<sub>3</sub>, and NH<sub>2</sub>OH productions can also be represented with a column vector,

$$R_T = (\nu_{1T}, \nu_{2T}, \dots, \nu_{mT})^T \quad (3)$$

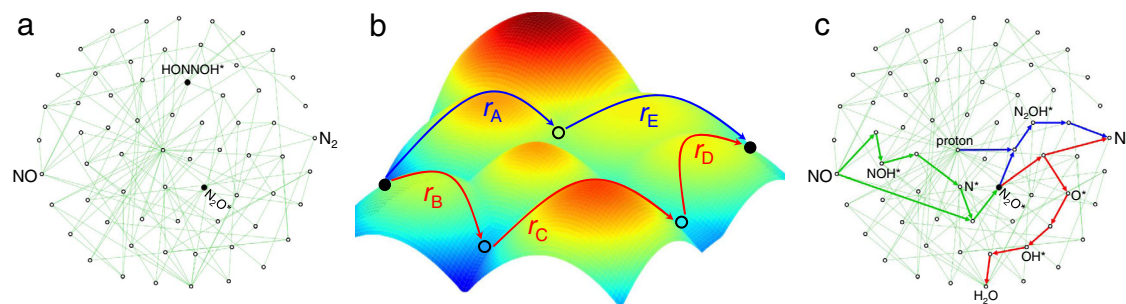


**Fig. 2** | **A scheme of determining the optimum pathways.** **a** The full reaction network for  $N_2$  production (constructed from Supplementary Table 1), where HONNOH\* and  $N_2O^*$  are the key intermediates of non- $N_2O^*$  and dis- $N_2O^*/p-N_2O^*$  paths (Supplementary Fig. 7), respectively. **b** The scheme of global energy

optimization. **c** Two optimal paths towards  $N_2$  via the further conversion of as-produced  $N_2O^*$ , where the common route from NO to  $N_2O^*$  is shown in thick green lines. The blue and red arrows connect the p- $N_2O^*$  and dis- $N_2O^*$  paths, respectively.

For a specific elementary step combination  $c_i = [\alpha_1, \alpha_2, \dots, \alpha_k]$ ,  $\alpha \in [1, \dots, n]$ , if it satisfies:

$$\text{Rank} \begin{pmatrix} \nu_{1\alpha_1} & \cdots & \nu_{m\alpha_1} \\ \vdots & \ddots & \vdots \\ \nu_{1\alpha_k} & \cdots & \nu_{m\alpha_k} \end{pmatrix} \geq k \quad (4)$$

$$\text{Rank} \begin{pmatrix} \nu_{1\alpha_1} & \cdots & \nu_{1\alpha_k} & \nu_{1T_j} \\ \vdots & \ddots & \vdots & \vdots \\ \nu_{m\alpha_1} & \cdots & \nu_{m\alpha_k} & \nu_{mT_j} \end{pmatrix} < k + 1 \quad (5)$$

The coefficient matrix will have only one solution  $p_i$ ,  $k \in [2, \dots, n]$ , which is the vector representative of pathway  $i$ . More details for this algorithm can be referred to in our previous work<sup>24</sup>. All enumerated reaction pathways for  $N_2$  production were summarized in Supplementary Table 2 and schematically shown in Supplementary Fig. 7.

To classify, the pathways of  $N_2$  production without  $N_2O^*$  involved are named non- $N_2O^*$ . In case  $N_2$  was produced via dissociation or protonation of as-produced  $N_2O^*$ , abbreviated as dis- $N_2O^*$  and p- $N_2O^*$ , respectively. Among all enumerated pathways, we first performed the internal comparison for a given path to determine the most difficult step,  $r_{\max}$ . Then, the minimum  $r_{\max}$  ( $\Delta G_{\text{RPD}}$ -limiting), identified from external comparison among all paths, can be used to describe the (quasi) activity, as shown in the following equation.

$$\Delta G_{\text{RPD}} - \text{limiting} = \min_i [\max_j (\Delta G_{(i,j)})] \quad (6)$$

where  $j$  and  $i$  represents the elementary steps of a given path and all possible paths, respectively. As shown in Fig. 2,  $r_C$  is the key step, instead of  $r_B$ , for the red path. The preference for blue and red paths is justified by the comparison between  $r_A$  and  $r_C$  steps. Hence, the  $\Delta G_{\text{RPD}}$ -limiting indicates a global optimization energy. As the  $r_{\max}$  evolves from one metal to another, the adsorption energies of all intermediates were calculated and correlated with one or two descriptors. Then, we can employ descriptors to establish a reaction phase diagram (RPD) to distinguish the reaction mechanism/phase<sup>24,25</sup>. The comparison and identification of the  $\Delta G_{\text{RPD}}$ -limiting (and selectivity-determining) steps were illustrated in Supplementary Figs. 8, 9. In addition, we have also considered the reaction pathways (Supplementary Table 3) for ammonia (Supplementary Fig. 10) and hydroxylamine productions to establish a general model for various products in eNORR.

The two-dimensional reaction phase diagrams (2D-RPDs) for eNORR to different products are shown in Fig. 3. The 2D-RPD is the overlapping of the (quasi) activity maps of all possible reaction paths.

Taking ammonia production as an example, the construction of 2D-RPD was illustrated in Supplementary Fig. 11. Figure 3a shows the (quasi) activity trend for  $N_2$  production, where all metals are not close to the optimum, indicating the low intrinsic activity of pure metals. Differently, Pd and Cu are nearly located at the optimum for  $N_2O$  (Fig. 3b) and  $NH_3$  (Fig. 3c) production, respectively. For the three products, the similarity is that the favorable pathways, separated into multiple regions by gray dotted lines, are diverse on different metals (Supplementary Table 4). However,  $NH_2OH$  production was found with the same mechanism over all studied metals (Supplementary Table 4), while the relatively strong chemical adsorption of  $NH_2OH^*$  limits its desorption (Fig. 3d), leading to low intrinsic activity towards hydroxylamine. It is quite consistent with the reported experiments<sup>27</sup> that hydroxylamine is always a minor product.

Overall, the  $\Delta G_{\text{RPD}}$ -limiting energies obtained by Fig. 3 can be used to estimate the activity trends of different products. Note that the number of electrons transferred towards different products ( $n_i$ ) affects the total current density ( $j_{\text{total}}$ ), so that an integrated descriptor  $\ln(\sum n_i e^{-\Delta G_i})$  was applied for the estimation of total activity. Figure 4 shows the comparisons between theoretical and experimental activity, where the colored points correspond to the different mechanisms in Fig. 3. The theoretical activities give basic agreement with experimental trends, verifying the mechanisms obtained by 2D-RPD analysis. As the  $\Delta G_{\text{RPD}}$ -limiting energies are close, some kinetic factors can influence the absolute activity. For instance, there are some deviations from Co, Ni, and Cu for the activity trends of  $N_2$  and  $N_2O$  productions (Fig. 4a, b). It can be attributed to the higher activity (larger current density) for ammonia production on Cu, resulting in relatively fewer NO contributions to  $N_2$  and  $N_2O$  productions, compared to Co and Ni. In the following, we will analyze the evolution of reaction mechanisms for  $N_2$  and  $N_2O$  production over all TMs to understand the fundamental limitations in  $N_2$  selectivity. For the comparison between  $N_2$  and  $N_2O$  productions in one-dimensional reaction phase diagram, we used abnormal scaling relations for more accurate energetic descriptions. More details are shown in Supplementary Fig. 12. Besides, the effects of potential and pH on  $N_2$  selectivity were studied on Pd, as it is the most active catalyst for electrochemical denitrification (Fig. 3a). The low  $N_2$  and  $N_2O$  activity on copper is discussed at the end in comparison with the primary ammonia production.

### Fundamental limitation in $N_2$ selectivity for all TMs

According to Fig. 5a, b,  $N_2$  is produced via  $N_2O^*$  over all studied metals. Because the formation of HONNOH\* (black dashed lines), a necessary step for non- $N_2O^*$  paths, is more difficult than  $N_2O^*$  protonation (blue dashed line) in left window and the key steps of  $N_2O^*$  dissociative mechanism (red dashed lines) in right window. More details for the evolution of favorable N-N coupling mechanism are shown in Supplementary Figs. 13, 14. Meanwhile, the mechanisms of  $N_2O$  production

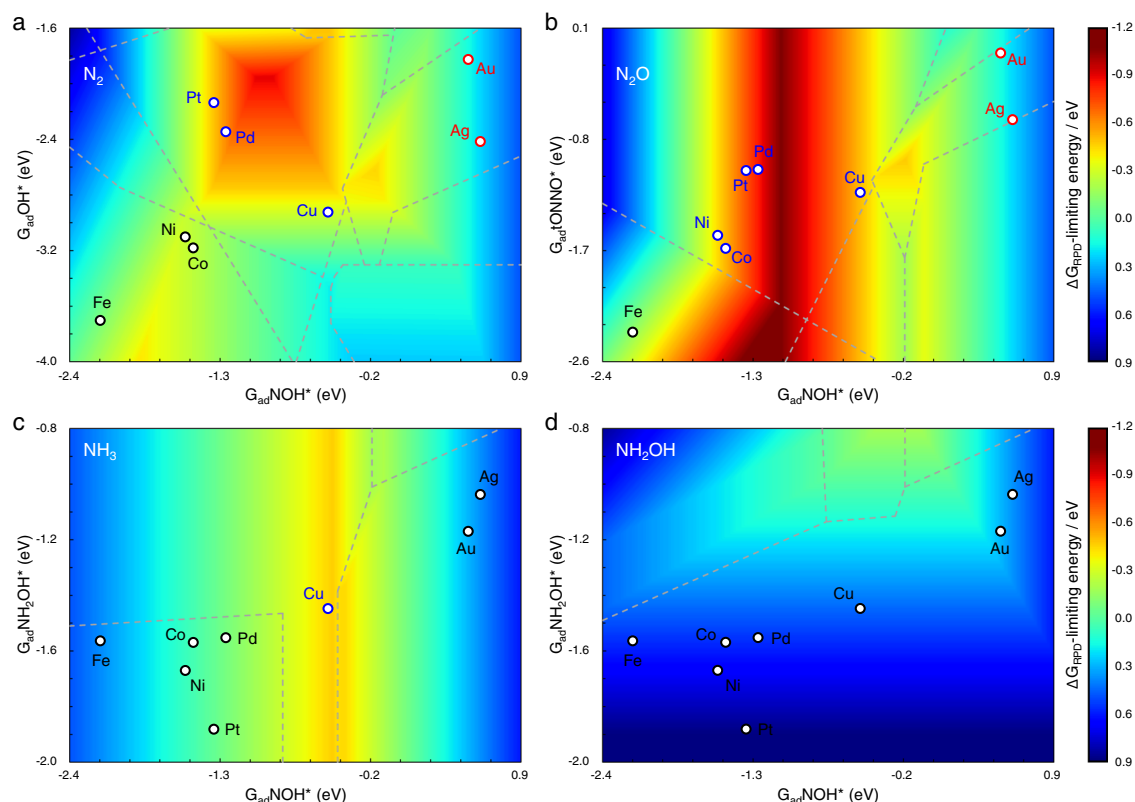


**Fig. 3 | The two-dimensional reaction phase diagrams (2D-RPDs).** a–d 2D-RPD for eNORR towards (a)  $N_2$ , (b)  $N_2O$ , (c)  $NH_3$ , and (d)  $NH_2OH$  at 0 V vs. RHE, where the windows with different mechanisms are divided by gray dotted lines (see details in

Supplementary Table 4).  $\Delta G_{RPD}$ -limiting energies are shown with reference to the color bar on the right.

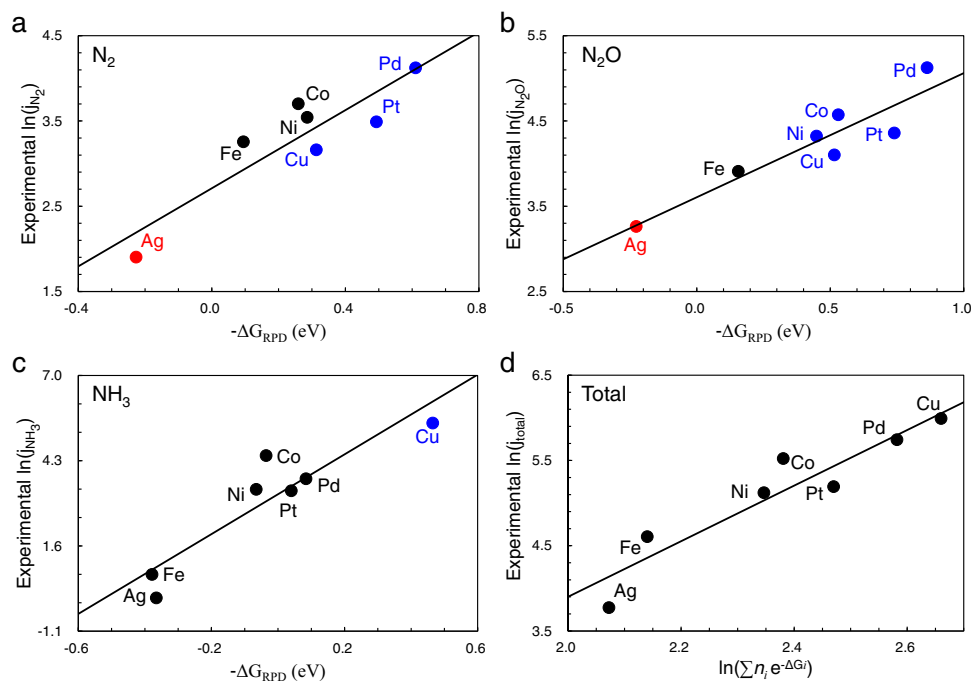


**Fig. 4 | The comparison between theoretical descriptor ( $-\Delta G_{RPD}$ ) and experimental activity<sup>17</sup> ( $\ln(j)$ ) at 0 V vs. RHE.** a–c The comparison between computational  $\Delta G_{RPD}$ -limiting energy and partial current density of (a)  $N_2$ , (b)  $N_2O$ , (c)  $NH_3$ .

d The total current density compared against the theoretical activity descriptor. The colored points correspond to the diverse mechanisms of different metals (Fig. 3).



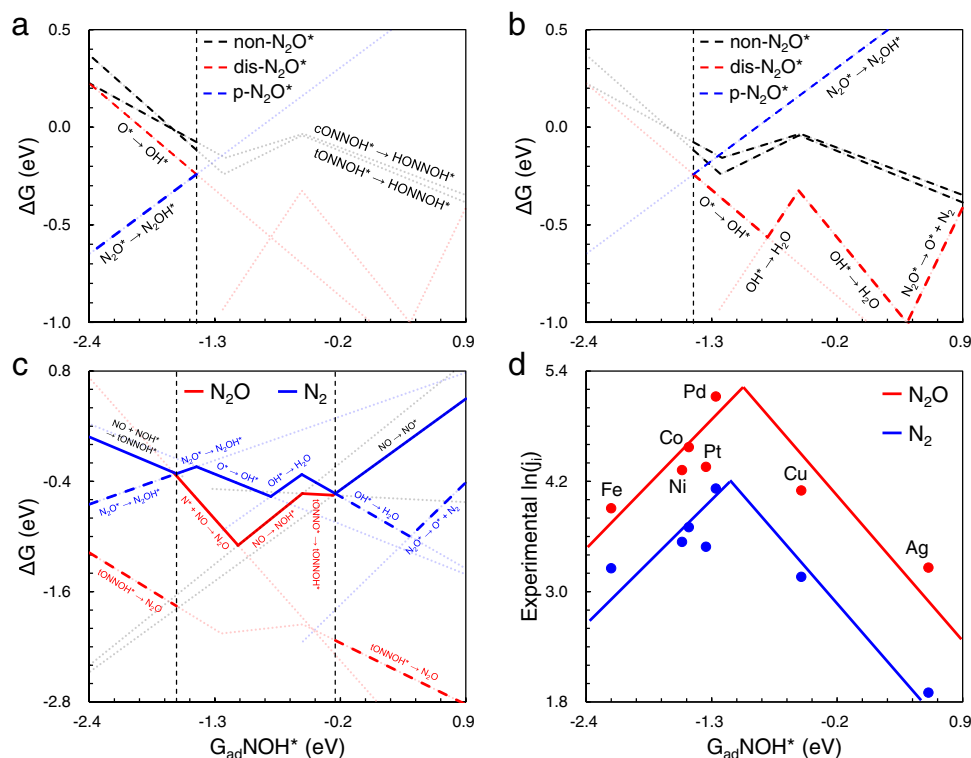


**Fig. 5 | The one-dimensional reaction phase diagrams (1D-RPDs) and activity trend for  $N_2$  and  $N_2O$  productions at 0 V vs. RHE. a, b** The path preference of (a) p- $N_2O^*$  (blue) on strongly reactive TMs ( $G_{ad}NOH^* < -1.46$  eV) and (b) dis- $N_2O^*$  (red) over others with  $G_{ad}NOH^*$  from  $-1.46$  to  $0.9$  eV, compared to non- $N_2O^*$  path (black), where the selective key steps are marked explicitly. **c** The selectivity

analysis for  $N_2$  and  $N_2O$  productions are colored in blue and red, respectively, where the  $\Delta G_{RPD}$ -limiting steps and key steps for product selection are shown in solid and dashed lines, respectively. **d** The measured activity trends (fitted blue and red lines) for  $N_2$  and  $N_2O$  productions<sup>17</sup>.

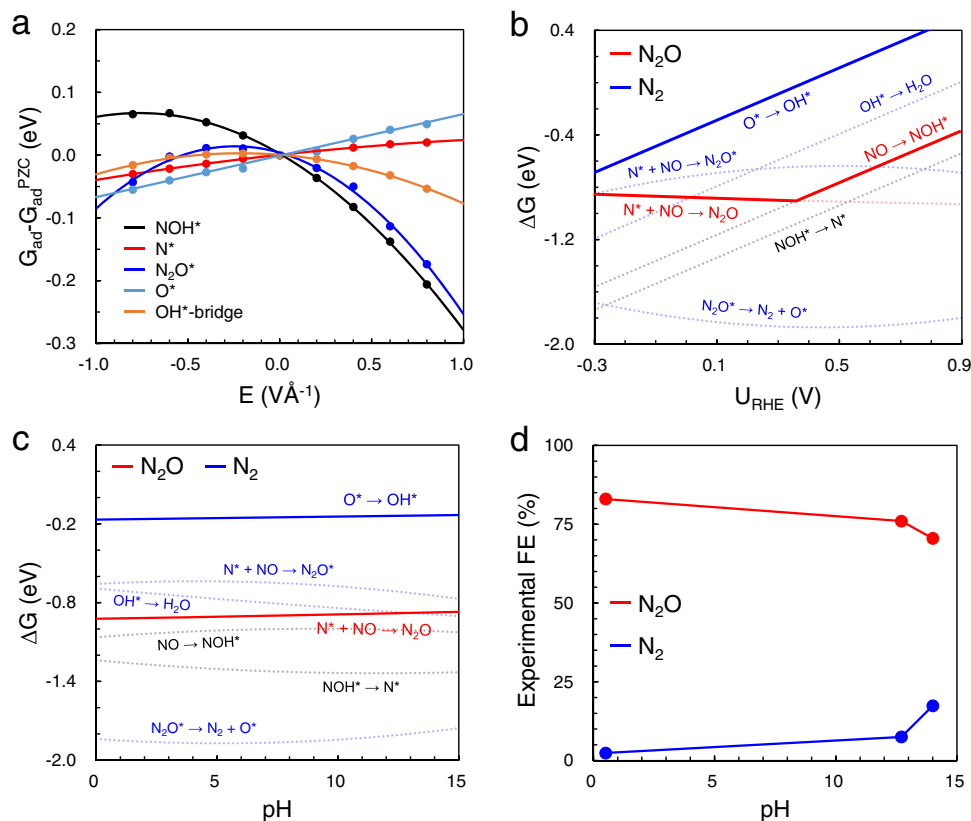
are explicitly shown in Supplementary Fig. 15. For the metals with strong adsorption ( $G_{ad}NOH^* < -1.46$  eV), the coupling of  $NOH^*$  and  $NO$  is more favorable than the other ways of N-N bond formation (Supplementary Fig. 13a–c). For these metals, such as Fe, Co and Ni, the activity is energetically limited by the reactions of  $NOH^*$  coupled with  $NO$  and  $N_2O^*$  protonation (Supplementary Fig. 14a). The  $\Delta G_{RPD}$ -limiting steps of dis- $N_2O^*$  path on other metals with weaker reactivity are the two-step protonation of  $O^*$  and  $NO$  adsorption (Supplementary Fig. 14b). For the moderately reactive metals like Pd and Cu, the N-N bond is most likely formed via the combination between  $N^*$  and  $NO$  (Supplementary Fig. 13d–f). As discussed in Supplementary Fig. 13g–i, the ER mechanism of  $NO^*$  coupled with  $NO$  is preferable on metals with the weakest adsorption (Au and Ag).

Figure 5c shows the key steps for product selectivity in three reaction phases. In general, over the metals in the left window,  $N_2$  and  $N_2O$  production share the same  $\Delta G_{RPD}$ -limiting step:  $NOH^*$  coupled with  $NO$  to  $tONNOH^*$ . In other words, the selectivity between  $N_2$  and  $N_2O$  production over Fe is determined by the secondary energetic determining steps, as shown in Supplementary Table 5. The follow-up dehydration of  $tONNOH^*$  on Fe directly releases  $N_2O$  ( $tONNOH^* \rightarrow N_2O$ ,  $\Delta G = -1.34$  eV). Compared to the  $N_2O$  release,  $N_2O^*$  protonation ( $N_2O^* \rightarrow N_2OH^*$ ,  $\Delta G = -0.55$  eV) is more difficult due to the (relatively) weak adsorption of  $N_2OH^*$ . The adsorption of  $N_2OH^*$  becomes weaker and weaker from left to right in 1D-RPD, giving rise to the exclusion of p- $N_2O$  paths on TMs with relatively weak reactivity. In the middle window, the  $\Delta G_{RPD}$ -limiting energies for  $N_2$  (blue solid lines) are higher than that of  $N_2O$  (red solid lines). It indicates the lower selectivity of  $N_2$  than  $N_2O$  production. Although the metals in the right window have equal  $\Delta G_{RPD}$ -limiting energies for the two products, the selectivity-determining steps, i.e.,  $N_2O^*$  dissociation and  $OH^*$  protonation, are much more difficult than  $N_2O$  release. For instance,  $N_2O^*$  dissociation

( $N_2O^* \rightarrow O^* + N_2$ ,  $\Delta G = -0.78$  eV) on Ag is more difficult than  $N_2O$  release ( $tONNOH^* \rightarrow N_2O$ ,  $\Delta G = -2.64$  eV). Supplementary Table 5 shows more details of energetic comparison on Ag. Hence, the reaction phase diagram explains well the lower  $N_2$  selectivity compared to  $N_2O$  production over all studied TMs.

In addition, the dis- $N_2O^*$  path is more preferable compared to p- $N_2O^*$  on Pd for  $N_2$  production, as shown in Fig. 5c. However, the  $N_2O$  production is the most favorable path with respect to both p- $N_2O^*$  and dis- $N_2O^*$  paths. In other words, we need to understand the energetic difference for the three limiting steps, namely,  $N^* + NO \rightarrow N_2O^*$  ( $-0.86$  eV),  $O^* \rightarrow OH^*$  ( $-0.34$  eV) and  $N_2O^* \rightarrow N_2OH^*$  ( $-0.15$  eV). It can be rationalized well by the projected density of states, as shown in Supplementary Fig. 16. First, as the  $NO$  molecule has unpaired electron at Fermi level, it can be strongly interacting with the  $N^*-2p$  states, resulting in a very stable N-N bond with the most stabilization of electronic states (Supplementary Fig. 16a). In contrast, the stabilization of  $N_2O^*$  by protonation is very limited since the  $N_2O^*$  has exhibited very stable electronic states (Supplementary Fig. 16b). In addition, as  $O^*$  has some unsaturated 2p states around the Fermi level (Supplementary Fig. 16c), but lower intensity compared to  $NO$ , whose stabilization by protonation is between the two cases above.

The experimental activity trend (Fig. 5d) for  $N_2$  and  $N_2O$  production over seven studied TMs indeed confirms our theoretical analysis above. The almost identical trends for the two products on all TMs greatly support our explanations that  $N_2$  is produced by  $N_2O^*$  further conversion. Besides, the lower  $N_2$  activity than  $N_2O$  in the whole reactivity window shows an excellent agreement with theoretical analysis of selectivity. Several previous works have also found similar phenomena that the  $N_2O$  production is dominant compared to  $N_2$  production<sup>8,11</sup>. In short, we identified two chemical origins for the low  $N_2$  selectivity. The first is that all TMs consistently bind  $N_2OH^*$



**Fig. 6 | Potential and pH effects on product selectivity.** **a** Field effects on intermediates involved in  $N_2$  and  $N_2O$  production on Pd. The fitted values of  $\mu$  (e Å) and  $\alpha$  (e Å<sup>2</sup> V<sup>-1</sup>) are shown in Supplementary Table 6. **b**, **c** The **(b)** potential-dependent and **(c)** pH-dependent (0.2 V vs. RHE) reaction free energies of steps in the optimum paths towards  $N_2$  and  $N_2O$  on Pd. The blue and red lines refer to steps for  $N_2$  and

$N_2O$  production, respectively, where the limiting steps are marked in bold. Note that the common steps ( $NO \rightarrow NOH^* \rightarrow N^*$ ) for the two products are shown in black. The  $OH^*$  is adsorbed at the bridge site, while the  $OH^*$  at the top and hollow sites are shown in Supplementary Fig. 17. **d** The experimental FE of  $N_2$  and  $N_2O$  on Pd, at 0.2 V vs. RHE<sup>17</sup>.

(relatively) too weakly. This inhibits the activity of  $N_2O^*$  protonation relative to its desorption. The second reason is that the scaling relation between  $O^*$  and  $OH^*$  on TMs limits their conversion or  $N_2O^*$  dissociation. This poisons the active sites for strongly reactive TMs. Meanwhile, it makes N-O bond breaking of  $N_2O^*$  difficult on metals with weak oxygen adsorption, resulting in a lower activity of  $N_2$  than  $N_2O$ . The two fundamental factors synergistically result in the low  $N_2$  selectivity on TMs.

### Potential and pH effects on $N_2$ selectivity

We now turn to another two influence factors, namely, electrode potential and electrolyte pH. The potential effects on the electrochemical process can be estimated by computational hydrogen electrode (CHE) model<sup>26</sup>. For thermochemical steps, the potential effect can be estimated through field effect on intermediates and transition states<sup>27</sup>, because an electric field exists at electrochemical interface. The intermediates can interact with the electric field due to their dipole moment and/or polarizability. The interaction will change their chemical potential and thus the corresponding reaction energies and barriers. Although it is difficult to directly measure the exact magnitude of the field, a reasonable approximation of linear correlation between electric field and absolute potential was reported previously<sup>28–30</sup>. Moreover, recent studies showed that the pH dependences can be explained well by field effect<sup>28,31,32</sup>. Thereby, the modeling of pH effects with an electric field (Eq. 13), as well as potential effect, are conducted in this section.

As mentioned above, the general order of major cathode products is dual-N products ( $N_2O/N_2$ ), single-N products ( $NH_3/NH_2OH$ ), and HER product ( $H_2$ ), from positive potentials to negative ones. Pd has been

theoretically and experimentally identified as the most active metal for dual-N products (Figs. 3a, b, 5d). Herein, we only focus on Pd and the low overpotentials ( $> -0.3$  V vs. RHE) to study potential and pH effects on  $N_2$  selectivity. According to intrinsic dipole moment ( $\mu$ ) and polarizability ( $\alpha$ ) (Supplementary Table 6), the response to the field of various intermediates relevant to  $N_2$  and  $N_2O$  productions was firstly calculated, as shown in Fig. 6a.  $G_{ad}^{PZC}$  refers to the adsorption-free energy at the potential of zero charge (PZC), corresponding to the energy calculated without applied field. Then, the reaction energies of N-N formation and N-O scission are corrected to different potentials, as shown in Fig. 6b. The insensitivity of  $N^*$  to field results in the  $N^*$ -NO coupling in  $N_2O$  production intact at potential  $< 0.4$  V vs. RHE. As the electrochemical steps are much more sensitive to potential than thermochemical ones, the  $O^* \rightarrow OH^*$  (limiting step for  $N_2$  production) is beneficial and faster by potential effects. However, the  $\Delta G_{RPD}$ -limiting energies of  $N_2$  production is still much larger than  $N_2O$  production. The difficult protonation of  $O^*$  causes the poison of active sites. In a word, the potential effects can slightly promote  $N_2$  production, consistent with experiments, but not enough to exceed  $N_2O$ .

At constant potential (RHE scale), an electrode at pH 12 have an absolute potential about 0.7 V lower than the one at pH 0. The difference in absolute potential leads to that the electrode at pH 12 exposed to an electric field nearly  $1 \text{ V Å}^{-1}$  stronger than the case at pH 0. In such electric field, the deviation of adsorbate binding energies could be an important contribution to the pH effect. Thus, pH dependence is proposed to originate from dependence on electric field, as clearly described in “Modeling pH effect with an electric field” paragraph. Figure 6c shows the pH effect on  $N_2$  and  $N_2O$  production at 0.2 V vs. RHE, where solid lines refer to the  $\Delta G_{RPD}$ -limiting steps. The field

insensitivity of  $N^*$  results in the activity towards  $N_2O$  intact at varying pH (red solid line). Besides, the dipole moments of  $OH^*$  (bridge site) and  $O^*$  species are very small, giving rise to the almost constant  $\Delta G_{RPD}$ -limiting energies (blue solid line:  $O^* \rightarrow OH^*$ ) for  $N_2$  production, which are much larger than that for  $N_2O$  production in the whole pH window. It suggests the lower  $N_2$  selectivity than  $N_2O$  at all pH, consistent with the experiments shown in Fig. 6d. In addition, the  $OH^*$ -Pd local structure has negative dipole moment and small polarizability response to electric field at hollow site, since it exhibits (almost) vertical adsorption structure. While the dipole moment is positive at top site due to the almost horizontal O-H bond (Supplementary Fig. 17). This means, the negative field can stabilize the  $OH^*$  on top site, while it destabilizes the ones at hollow site, as shown in Supplementary Fig. 17a. Supplementary Fig. 17b shows that the  $O^* \rightarrow OH^*$  is more favorable at hollow site in acidic condition. Instead, the  $O^* \rightarrow OH^*$  at top site can enhance the activity in alkaline condition. Moreover, the  $OH^*$  coverage is relatively lower at acidic condition. It should be dominant by the more favorable  $OH^*$  at bridge and hollow sites. At alkaline condition, the  $OH^*$  coverage should be higher and with more  $OH^*$  at top site. Therefore, the  $N_2$  production can be further enhanced at alkaline condition from  $OH^*$  at top sites (Supplementary Fig. 17b).

Certainly, the energetic difference from the  $OH^*$  adsorption sites is small. Another important influence factor should be that the  $N_2O^*$  adsorption becomes more stable at alkaline condition (Fig. 6a). In other words, the local pressure/concentration of  $N_2O$  can be higher at alkaline condition. As the lifetime of  $N_2O$  at electrochemical interface becomes longer, it will enhance the second conversion of as-produced  $N_2O$ . As shown in Fig. 1, the Faradaic efficiency of  $N_2$  and  $N_2O$  production can fluctuate by  $\sim 15\%$  at varying NO partial pressures. We believe the local pressure or concentration of  $N_2O$  can also change the Faradaic efficiency with the comparable magnitude. In addition, surface engineering of electrode can be another possibility to enhance the activity or selectivity. The  $H^*$ -covered Pd and new Pd-based materials should be possible to improve  $N_2$  selectivity. However, it is very hard to form a high  $H^*$  coverage because the  $NO^*$  adsorption is always stronger than  $H^*$  (Supplementary Fig. 18). Although it is very unfavorable to form PdH above 0 V vs. RHE, it might be possible at very negative potentials. Hence, we calculated the activity and selectivity of eNORR to  $N_2$  production on  $H^*$ -covered Pd and PdH. Details for the models are shown in Supplementary Figs. 19, 20. As shown in Supplementary Fig. 21a, it was found the activity of  $N_2$  production was lower compared to Pd. Besides, the  $N_2$  selectivity was lower than  $N_2O$  over all studied materials (Supplementary Fig. 21b). It indicates that  $H^*$ -modified Pd cannot realize a higher  $N_2$  activity and selectivity. Moreover, we have calculated the activity of  $N_2$  and  $N_2O$  production over six Pd-based alloys (Supplementary Fig. 22). However, it fails to find a candidate with higher  $N_2$  selectivity against  $N_2O$  production (Supplementary Fig. 23).

### An exceptional selectivity over copper

Cu is exceptional to all other TMs and favors ammonia production with very low selectivity, not only for  $N_2$ , but also  $N_2O$  production. As shown in Supplementary Fig. 24, ammonia production indeed has comparable energies in limiting steps with  $N_2O$  production on copper. For strongly reactive catalysts, the  $N_2O$  production is much favorable with respect to ammonia production. The previous work has also found that NO protonation has a larger barrier than its adsorption over weakly reactive catalysts, for instance, 0.4 eV on Ag<sup>23</sup>. This indicates most TMs should be  $N_2O$ -selective and Cu is exceptional in selectivity. Indeed, the experimental selectivity (Supplementary Fig. 25) is consistent with our thermodynamic analysis.

In addition, we built a microkinetic model to study the potential and electric effects. The barriers for  $N_2O$  and  $NH_3$  production were explicitly calculated in our previous work<sup>19</sup>. For proton-electron coupled transfer reactions, a monolayer of water containing a hydronium ( $H_3O^+$ ) was explicitly added on the Cu(111) surface. The

electrochemical barriers were extrapolated to a given electrode potential with the charge-extrapolation scheme based on a capacitor model<sup>33,34</sup>. More computational details of potential-dependent barriers are given in Eqs. 14 and 15. Towards  $N_2$ , the dissociative barrier of  $N_2O^*$  to  $N_2 + O^*$  (Supplementary Fig. 4) and the two-step protonation barriers of  $O^*$  to  $H_2O$  (Supplementary Fig. 26) were also calculated in this work. The pH effect can be diverse and complex in kinetics. A major contribution from electric field (Fig. 7a) was considered in our model.

To compare with the previous experiments<sup>19</sup>, the microkinetic modelings were performed at pH 7.0, employing the corrected energetics listed in Supplementary Table 7. Following Arrhenius equation, the rate constants were computed at different potentials. According to the steady-state approximation<sup>35</sup>, the surface coverage ( $\theta$ ) of adsorbates for  $NH_3$  and  $N_2/N_2O$  production was solved at varying potentials, respectively. More details can be found in "Microkinetic modeling" paragraph. Correspondingly, the intrinsic activity for  $NH_3$  or  $N_2/N_2O$  can be theoretically estimated. In the wide potential region from 0.3 to  $-1.2$  V, the Faradaic efficiency of  $NH_3$  is much higher than  $N_2$  and  $N_2O$ , which shows a great agreement with experimental trends (Fig. 7b, insert).

The production of  $NH_3$  and  $N_2/N_2O$  have similar apparent activation barriers at all studied potentials, as shown in Supplementary Fig. 27a. It suggests that  $NH_3$  production has no obvious superiority at kinetic barriers. The high selectivity of  $NH_3$  should be attributed to preferable (total) thermodynamics, as reflected from the surface coverage of key intermediates. The degree of rate control (DRC) for elementary steps ( $X_{RC}$ ) was analyzed, which reflects the influence of a given step on the overall reaction<sup>36,37</sup>. The rate-determining step (RDS) is defined as the step with the largest  $X_{RC}$ . As the RDS for  $NH_3$  production (Supplementary Fig. 27b), the electrochemical dehydration of  $NOH^*$  to  $N^*$ , is also a necessary step for  $N_2/N_2O$  production. The conversion of  $N^*$  is the key step for the selectivity towards different products, the rate of which influences the surface coverage of  $NOH^*$  ( $\theta_{NOH^*}$ ) at steady-state. For ammonia production, the continuous protonation of  $N^*$  is faster, giving rise to low  $\theta_{N^*}$  and thus high  $\theta_{NOH^*}$  (Fig. 7c). However, the sluggish coupling of  $N^*$  and NO makes the active site mainly covered by  $N^*$  for  $N_2/N_2O$  production, leading to low  $\theta_{NOH^*}$ . A lower  $\theta_{NOH^*}$  indicates a slower rate of NO conversion. This indicates that the exceptionally high ammonia selectivity on Cu can be attributed to facile  $N^*$  protonation. Another influence factor, partial pressure of NO, was tested from 0.001 to 1 at 0.3 V vs. RHE. The results (Supplementary Fig. 27c) did not show the reversal of selectivity, although a high NO pressure facilitates the N-N coupling reaction. In addition, the selectivity between  $N_2$  and  $N_2O$  can be understood by DRC analysis. As shown in Fig. 7d, the RDS for  $N_2$  is always the dissociation of  $N_2O^*$ , which is more difficult than the barrierless desorption of  $N_2O^*$ . The slower dissociation of  $N_2O^*$  results in a lower  $N_2$  selectivity over copper.

Therefore, we would propose to make efforts in the following four directions. (1) To design the catalysts with distinctly strong  $N_2OH^*$  adsorption (breaking scaling relation) or discover an alternative class of materials, instead of TMs, this is a possible solution for enhancing the  $N_2$  selectivity with respect to  $N_2O$  production. (2) Although the choice/engineering of electrodes is demonstrated to be very difficult to enhance  $N_2$  selectivity, the design of the reactor can be considered as another factor. For instance, a high  $N_2$  selectivity with respect to  $N_2O$  production was achieved<sup>11-13</sup>, where the electrode has a much larger surface area and the NO flow rate is low instead. Towards high  $N_2$  selectivity, it should be a feasible route to construct a cascade reactor via the combination of NO-to- $N_2O$  and  $N_2O$ -to- $N_2$ , as the direct  $N_2O$  electroreduction to  $N_2$  is highly efficient<sup>17</sup>. (3) To enhance the efficiency of thermochemical steps, it can be achieved by reducing the accessibility of proton to suppress electrochemical steps, for instance, by using non-aqueous proton donor<sup>38-41</sup>. (4) At last, we can also steer from electrochemical denitrification to ammonia synthesis as the latter is a fundamentally more feasible route based on Cu-based catalysts.

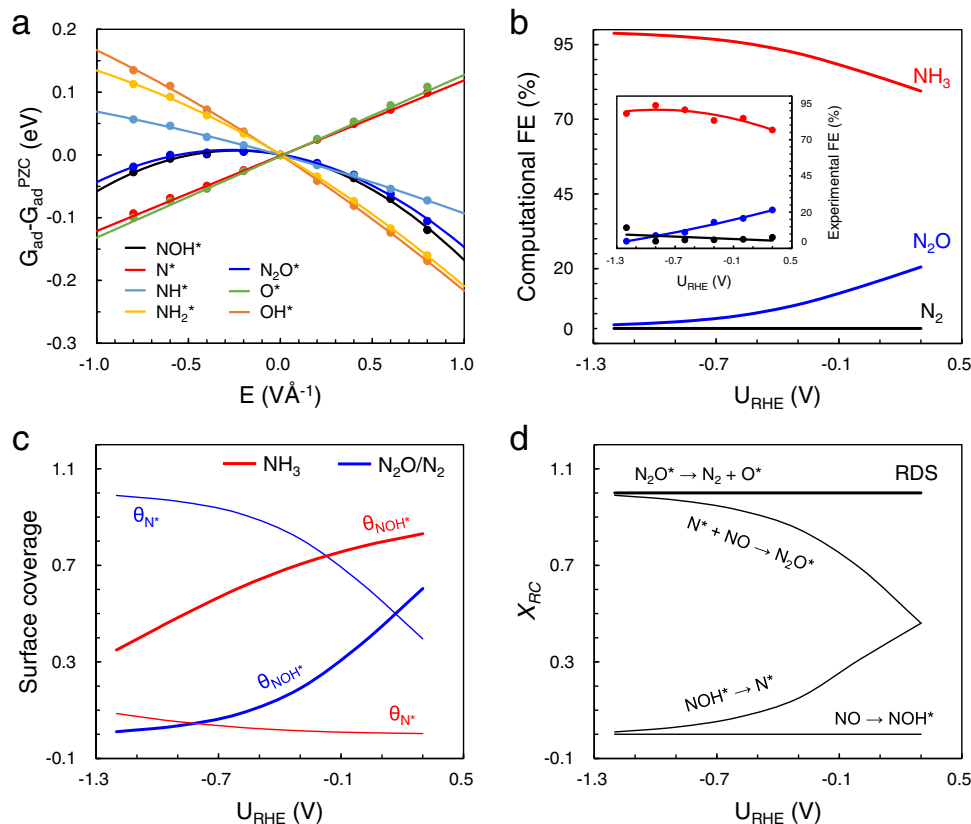


**Fig. 7 | The results of microkinetic modeling on Cu. a** Field effect on the adsorption energies of relevant intermediates in eNORR on Cu. **b** The computational and experimental (insert)<sup>19</sup> FE of different products for eNORR on Cu. **c** The surface coverage of key intermediates in the formation of NH<sub>3</sub> (red lines) and dual-

N products (blue lines). **d** Degree of rate control (DRC) of different elementary steps ( $X_{RC}$ ) for N<sub>2</sub> production, where the rate-determining step (RDS) is shown in a thick line.

The eNORR route can also serve as an electrochemical platform for amination.

## Discussion

As discussed above, the low N<sub>2</sub> selectivity in eNORR originates from two aspects. On the one hand, the surface reactivity of all TMs is very disadvantageous to N<sub>2</sub> production from the energetic point of view. Firstly, TM surfaces consistently bind N<sub>2</sub>OH\* too weakly, inhibiting the activity of N<sub>2</sub>O\* protonation relative to its desorption. Secondly, the scaling relation between O\* and OH\* makes the active sites on strong reactive TM surface poisoned by O\*/OH\* or causes N<sub>2</sub>O\* dissociation very difficult on metals with weak adsorption. The two natures synergistically make all TMs more N<sub>2</sub>O-selective. Note that the key factor for high NH<sub>3</sub> selectivity on Cu is the facile N\* protonation. On the other hand, the optimization of experimental conditions, such as potential, pH and NO pressure, can slightly promote N<sub>2</sub> selectivity, but not enough to exceed N<sub>2</sub>O or NH<sub>3</sub>, as observed experimentally. The comparisons between experimental and theoretical results indicate the activity trend for various products can be well described by the reaction phase diagram. The insights for low N<sub>2</sub> selectivity in eNORR can be a guideline for the future design of catalysts. More importantly, the exceptional activity of ammonia production provided a feasible route to build up a reverse artificial nitrogen cycle, which can play a critical role for decentralized ammonia synthesis with sustainable electricity.

## Methods

### Computational details

DFT calculations were performed using Vienna Ab initio Simulation Package (VASP)<sup>42–44</sup>. All calculations were conducted at the level of

generalized gradient approximation (GGA)<sup>45</sup> with the revised Perdew-Burke-Ernzerhof<sup>46</sup> functional. The projected augmented wave (PAW)<sup>47,48</sup> method was used. Spin-polarized calculations were made to Fe, Co, and Ni and the rest metals are spin restricted. A kinetic energy cutoff of 400 eV was used in this work. Structural optimizations were performed with the residual force and electronic energy differences smaller than  $-0.05$  eV/Å and  $10^{-5}$  eV, respectively. The van der Waals corrections<sup>49,50</sup> were considered by DFT-D3 method. To calculate the adsorption energies for different adsorbates, the energies of gas-phase N<sub>2</sub>, H<sub>2</sub>, and NO were used as references. For free energy correction<sup>51</sup>, in terms of zero-point energy and entropic (S) contribution, electronic energies were corrected at the experimental temperature ( $T = 298$  K), where the vibrational entropy for adsorbed intermediates while translational, rotational, and vibrational motions for gases were considered, respectively. To locate transition states, the climbing image nudged elastic band (CI-NEB) scheme<sup>52</sup> and dimer method<sup>53,54</sup> were employed.

For atomic models, a close-packed bcc(110) surface was used to model the flat surface of Fe metal, while fcc(111) surfaces were used for Co, Ni, Pt, Pd, Cu, Au, and Ag. Four-layer  $3 \times 8$  supercell was constructed for bcc(110) surface of Fe, and  $4 \times 6$  slabs were established for other metals. The adsorbates were permitted to relax with the two top-layer metal atoms, while the two bottom layers were fixed. Besides, a vacuum region of  $-15$  Å was introduced along the z-direction to avoid interactions between images. All slabs were optimized by a Monkhorst-Pack k-point of  $2 \times 2 \times 1$ . The scheme of Methfessel-Paxton<sup>55</sup> ( $N = 1$ ) was used for the smearing width of 0.2 eV. Moreover, the solvation (Supplementary Tables 8 and 9) and field effect on adsorption energy of intermediates were considered in DFT calculations. Electric fields were applied using a saw-tooth potential corresponding to fields between



−0.8 and 0.8 VÅ<sup>−1</sup>. All adsorbates were relaxed at each applied field, which was used to predict their response to field.

### Modeling response of adsorbates to electric field

The response of adsorbed intermediates to the field can be measured by the fitted second-order polynomial:

$$G_{\text{ad}} = G_{\text{ad}}^{\text{PZC}} + \mu \mathbf{E} - \frac{\alpha}{2} \mathbf{E}^2 \quad (7)$$

where  $\mathbf{E}$  is the applied field and  $G_{\text{ad}}^{\text{PZC}}$  refers to the adsorption-free energy at potential of zero charge (PZC), corresponding to the energy calculated with no applied field. Here,  $\mu$  and  $\alpha$  represent the intrinsic dipole moment and polarizability of adsorbates, respectively. By fitting calculated ( $G_{\text{ad}} - G_{\text{ad}}^{\text{PZC}}$ ) with field  $\mathbf{E}$ ,  $\mu$  and  $\alpha$  of each intermediates can be determined. Furthermore, based on a parallel-plate capacitor model, a linear correlation between electric field and absolute potential was approximated as following:

$$\mathbf{E} = \frac{\sigma}{\varepsilon \varepsilon_0} = \frac{C_{\text{H}}(U_{\text{SHE}} - U_{\text{PZC}})}{\varepsilon \varepsilon_0} \quad (8)$$

where  $\sigma$  is the surface charge density,  $\varepsilon$  and  $\varepsilon_0$  are the dielectric constant of vacuum and water near interface, which were set to be  $8.85 \times 10^{-12} \text{ F m}^{-1}$  and 2 (unitless), respectively.  $C_{\text{H}}$  refers to Helmholtz capacitance ( $\mu\text{F cm}^{-2}$ ), which can vary with the surface and potential but ranged between 20 and  $60 \mu\text{F cm}^{-2}$ <sup>28,56,57</sup>. We used a constant  $C_{\text{H}}$  of  $25 \mu\text{F cm}^{-2}$  across all surfaces and potential<sup>28</sup>.  $U_{\text{SHE}}$  is the electrode potential referenced to standard hydrogen electrode (SHE).  $U_{\text{PZC}}$  refers to the potential at PZC versus SHE. The experimental values of 0 and 0.09 V were used for  $U_{\text{PZC}}$  on Pd and Cu<sup>58</sup>.

### Modeling pH effect with an electric field

As described by Eq. 8, the electric field depends on the absolute potential of an electrode. It can be measured by using a standard hydrogen electrode ( $U_{\text{SHE}}$ ), which relates to RHE (reversible hydrogen electrode) by Eq. 9.

$$U_{\text{SHE}} = U_{\text{RHE}} - k_{\text{B}} T \ln(10) \times (\text{pH}) = U_{\text{RHE}} - 0.059 \text{pH} \quad (9)$$

Thus, electric field dependencies manifest themselves as dependencies on pH when viewed on an RHE scale. In detail, according to Eqs. 7, 8, the effect of electrode potential on intermediates adsorption energy can be estimated by the following mathematical expression:

$$G_{\text{ad}} = G_{\text{ad}}^{\text{PZC}} + \mu \frac{C_{\text{H}}}{\varepsilon \varepsilon_0} (U_{\text{SHE}} - U_{\text{PZC}}) - \frac{\alpha}{2} \left( \frac{C_{\text{H}}}{\varepsilon \varepsilon_0} \right)^2 (U_{\text{SHE}} - U_{\text{PZC}})^2 \quad (10)$$

At a given RHE potential and varying pH, Eq. 10 has new expressions as Eqs. 11 and 12:

$$G_{\text{ad}}^{\text{pH}=0} = G_{\text{ad}}^{\text{PZC}} + \mu \frac{C_{\text{H}}}{\varepsilon \varepsilon_0} (U_{\text{RHE}} - U_{\text{PZC}}) - \frac{\alpha}{2} \left( \frac{C_{\text{H}}}{\varepsilon \varepsilon_0} \right)^2 (U_{\text{RHE}} - U_{\text{PZC}})^2 \quad (11)$$

$$G_{\text{ad}}^{\text{pH}} = G_{\text{ad}}^{\text{PZC}} + \mu \frac{C_{\text{H}}}{\varepsilon \varepsilon_0} (U_{\text{RHE}} - U_{\text{PZC}}) - \frac{\alpha}{2} \left( \frac{C_{\text{H}}}{\varepsilon \varepsilon_0} \right)^2 (U_{\text{RHE}} - U_{\text{PZC}})^2 + \mu \frac{C_{\text{H}}}{\varepsilon \varepsilon_0} (-0.059 \text{pH}) - \frac{\alpha}{2} \left( \frac{C_{\text{H}}}{\varepsilon \varepsilon_0} \right)^2 (-0.059 \text{pH})^2 \quad (12)$$

Here, we see that the adsorption energy of an adsorbate can be split into three contributions: the intrinsic binding strength of the catalysts described by  $G_{\text{ad}}^{\text{PZC}}$ , the RHE potential dependence, and pH dependence described by the  $\mu$  and  $\alpha$  terms. In short, the brief formula

for modeling pH effect with an electric field is shown as Eq. 13.

$$G_{\text{ad}}^{\text{pH}} = G_{\text{ad}}^{\text{pH}=0} + \mu \frac{C_{\text{H}}}{\varepsilon \varepsilon_0} (-0.059 \text{pH}) - \frac{\alpha}{2} \left( \frac{C_{\text{H}}}{\varepsilon \varepsilon_0} \right)^2 (-0.059 \text{pH})^2 \quad (13)$$

### Microkinetic modeling

The potential-dependent barriers ( $G_{\text{a}}$ ) of proton-electron coupled transfer reactions were calculated by “charge-extrapolation” method<sup>33,34</sup>. As proton source, a monolayer water containing a hydronium ( $\text{H}_3\text{O}^+$ ) was placed on the surface. According to a capacitor model, the barriers can be extrapolated to a given electrode potential based on the work function variations, as described in the following equations:

$$G_{\text{a}}(\Phi_{\text{IS}}) = G_{\text{TS}}(\Phi_{\text{IS}}) - G_{\text{IS}}(\Phi_{\text{IS}}) = G_{\text{TS}}(\Phi_{\text{TS}}) - G_{\text{IS}}(\Phi_{\text{IS}}) + \frac{(q_{\text{TS}} - q_{\text{IS}})(\Phi_{\text{TS}} - \Phi_{\text{IS}})}{2} \quad (14)$$

$$G_{\text{a}}(\Phi_{\text{TS}}) = G_{\text{TS}}(\Phi_{\text{TS}}) - G_{\text{IS}}(\Phi_{\text{TS}}) = G_{\text{TS}}(\Phi_{\text{TS}}) - G_{\text{IS}}(\Phi_{\text{IS}}) - \frac{(q_{\text{TS}} - q_{\text{IS}})(\Phi_{\text{TS}} - \Phi_{\text{IS}})}{2} \quad (15)$$

where  $G_{\text{IS}}(\Phi_{\text{IS}})$  and  $G_{\text{TS}}(\Phi_{\text{TS}})$  are corresponding to the free energies of initial and transition states, respectively.  $\Phi$  and  $q$  refer work function and charge change of water layer, respectively. Accordingly, the slope of  $G_{\text{a}}$  changing with potential ( $\Phi$ ), i.e. charge transfer coefficient  $\beta$ , was computed by taking Eqs. 14, 15 and approximated to be constant. A specific  $\Phi$  corresponds to an electrode potential (vs. SHE) by following equation:

$$U_{\text{SHE}} = \frac{\Phi - \Phi_{\text{SHE}}}{e} \quad (16)$$

where  $\Phi_{\text{SHE}}$  was detected experimentally to be −4.4 eV. By the scheme above, the potential-dependent  $G_{\text{a}}$  of electrochemical steps towards  $\text{NH}_3$  and  $\text{N}_2\text{O}$  were calculated, as reported in our previous work<sup>19</sup>. Towards  $\text{N}_2$ , the dissociative barrier of  $\text{N}_2\text{O}^*$  to  $\text{N}_2 + \text{O}^*$  and the two-step protonation barriers of  $\text{O}^*$  to  $\text{H}_2\text{O}$  were calculated in this work.

The microkinetic modeling of eNORR on Cu was based on the method by JianFu Chen and HaiFeng Wang, using the CATKINAS package<sup>59</sup>. To study the intrinsic activity for  $\text{NH}_3$  and dual-N products ( $\text{N}_2/\text{N}_2\text{O}$ ), microkinetic simulations were conducted at two sites. The surface coverage ( $\theta$ ) of adsorbates was solved with the steady-state approximation. The rates for elementary reactions were calculated using the follow-up equation:

$$\text{rate} = k_{\text{f}} \prod \theta_{\text{react}} - k_{\text{b}} \prod \theta_{\text{prod}} \quad (17)$$

where  $\theta_{\text{react}}$  and  $\theta_{\text{prod}}$  refer to the coverages of reactants and products, respectively. The reaction constants  $k_{\text{f}}$  and  $k_{\text{b}}$ , respectively, reflect the degree of difficulty of forward and backward reactions, which was calculated by Arrhenius equation:

$$k = A e^{-\frac{G_{\text{a}}}{k_{\text{B}} T}} \quad (18)$$

where  $A$  ( $\text{s}^{-1}$ ),  $G_{\text{a}}$ ,  $k_{\text{B}}$  and  $T$  are reaction prefactor, activation free energy, Boltzmann constant and reaction temperature, respectively.

In this work, microkinetic modeling was performed at 298 K and an RHE potential region from 0.3 to −1.2 V. The partial pressure of NO was firstly tested from 0.001 to 1 at 0.3 V (Supplementary Fig. 27c) and finally set to be 0.1 atm due to the very low solubility of NO in aqueous solution. Besides, the partial pressure of products ( $\text{N}_2$ ,  $\text{N}_2\text{O}$ , and  $\text{NH}_3$ ) was set at 0.01 atm due to the relatively low yield rate. All energetics

employed for microkinetic modeling are listed in Supplementary Table 7.

The computational Faradaic efficiency for each product was calculated by the following equation:

$$FE(\%) = \frac{n_i TOF_i}{\sum n_i TOF_i} \times 100\% \quad (19)$$

where  $n_i$  refers to the total electron transfer number and  $TOF_i$  represents the turnover frequency obtained by microkinetic modeling for product  $i$ .

## Data availability

The optimized structures of Pd-based alloys and PdH surfaces are provided in Supplementary dataset 1. Besides, all data that support the findings of this study are presented in the main text and Supplementary information, where the source data of Figs. 1, 3, 4, 6, and 7 are listed in Supplementary dataset 2. The additional datasets are available from the corresponding author upon reasonable request.

## Code availability

The VASP used for DFT calculations is available from the website <https://www.vasp.at/>, and the CATKINAS package used for microkinetic modeling is available from the website <https://www.catkinas.com/>. For both simulation techniques, input and output files are available from the corresponding author upon reasonable request.

## References

- TsungYu, L. & Hsunling, B. Low temperature selective catalytic reduction of NO<sub>x</sub> with NH<sub>3</sub> over Mn-based catalyst: a review. *AIMS Environ. Sci.* **3**, 261–289 (2016).
- Roy, S., Hegde, M. S. & Madras, G. Catalysis for NO<sub>x</sub> abatement. *Appl. Energy* **86**, 2283–2297 (2009).
- Whipple, D. T. & Kenis, P. J. A. Prospects of CO<sub>2</sub> utilization via direct heterogeneous electrochemical reduction. *J. Phys. Chem. Lett.* **1**, 3451–3458 (2010).
- Ko, B. H. et al. The impact of nitrogen oxides on electrochemical carbon dioxide reduction. *Nat. Commun.* **11**, 5856 (2020).
- Koebel, M., Madia, G. & Elsener, M. Selective catalytic reduction of NO and NO<sub>2</sub> at low temperatures. *Catal. Today* **73**, 239–247 (2002).
- Rosca, V. et al. Nitrogen cycle electrocatalysis. *Chem. Rev.* **109**, 2209–2244 (2009).
- de Vooy, A. C. A. et al. Mechanisms of electrochemical reduction and oxidation of nitric oxide. *Electrochim. Acta* **49**, 1307–1314 (2004).
- de Vooy, A. C. A. et al. Mechanistic study of the nitric oxide reduction on a polycrystalline platinum electrode. *Electrochim. Acta* **46**, 923–930 (2001).
- Beltramo, G. L. & Koper, M. T. M. Nitric oxide reduction and oxidation on stepped Pt[n(111)×(111)] electrodes. *Langmuir* **19**, 8907–8915 (2003).
- Gootzen, J. F. E. et al. The study of NO adsorbate layers on platinumized platinum in the liquid phase with cyclic voltammetry, DEMS and FTIRS. *Recl. Trav. Chim. Pays-Bas* **115**, 480–485 (1996).
- Shibata, M., Murase, K. & Furuya, N. Reduction of nitrogen monoxide to nitrogen at gas diffusion electrodes with noble metal catalysts. *J. Appl. Electrochem.* **28**, 1121–1125 (1998).
- Hara, K. et al. Electrocatalytic reduction of NO on metal electrodes and gas diffusion electrodes in an aqueous electrolyte. *J. Electroanal. Chem.* **451**, 181–186 (1998).
- de Vooy, A. C. A. et al. Mechanistic study on the electrocatalytic reduction of nitric oxide on transition-metal electrodes. *J. Catal.* **202**, 387–394 (2001).
- Otsuka, K., Sawada, H. & Yamanaka, I. A hydrogen-nitric oxide cell for the synthesis of hydroxylamine. *J. Electrochem. Soc.* **143**, 3491–3497 (1996).
- Colucci, J. A., Foral, M. J. & Langer, S. H. Nitric oxide reduction at noble metal electrodes: a voltammetric study in acid solution. *Electrochim. Acta* **30**, 1675–1685 (1985).
- Janssen, L. J. J., Pieterse, M. M. J. & Barendrecht, E. Reduction of nitric oxide at a platinum cathode in an acidic solution. *Electrochim. Acta* **22**, 27–30 (1977).
- Ko, B. H. et al. Electrochemical reduction of gaseous nitrogen oxides on transition metals at ambient conditions. *J. Am. Chem. Soc.* **144**, 1258–1266 (2022).
- Kim, D. et al. Unveiling electrode-electrolyte design-based NO reduction for NH<sub>3</sub> synthesis. *ACS Energy Lett.* **5**, 3647–3656 (2020).
- Long, J. et al. Direct electrochemical ammonia synthesis from nitric oxide. *Angew. Chem. Int. Ed. Engl.* **59**, 9711–9718 (2020).
- Clayborne, A. et al. Elucidation of pathways for NO electroreduction on Pt(111) from first principles. *Angew. Chem. Int. Ed. Engl.* **54**, 8255–8258 (2015).
- Chun, H.-J. et al. Atomistic insights into nitrogen-cycle electrochemistry: a combined DFT and kinetic monte carlo analysis of NO electrochemical reduction on Pt(100). *ACS Catal.* **7**, 3869–3882 (2017).
- Chun, H.-J., Zeng, Z. & Greeley, J. DFT insights into NO electrochemical reduction: a case study of Pt(211) and Cu(211) surfaces. *ACS Catal.* **12**, 1394–1402 (2022).
- Long, J. et al. Unveiling potential dependence in NO electroreduction to ammonia. *J. Phys. Chem. Lett.* **12**, 6988–6995 (2021).
- Fu, X. et al. Understanding the product selectivity of syngas conversion on ZnO surfaces with complex reaction network and structural evolution. *ACS Catal.* **11**, 12264–12273 (2021).
- Guo, C. et al. Toward computational design of chemical reactions with reaction phase diagram. *WIREs Comput. Mol. Sci.* **11**, No. e1514 (2021).
- Nørskov, J. K. et al. Origin of the overpotential for oxygen reduction at a fuel-cell cathode. *J. Phys. Chem. B* **108**, 17886–17892 (2004).
- Chen, L. D. et al. Electric field effects in electrochemical CO<sub>2</sub> reduction. *ACS Catal.* **6**, 7133–7139 (2016).
- Kelly, S. R. et al. Electric field effects in oxygen reduction kinetics: rationalizing pH dependence at the Pt(111), Au(111), and Au(100) electrodes. *J. Phys. Chem. C* **124**, 14581–14591 (2020).
- Takasu, Y., Yoshinaga, N. & Sugimoto, W. Oxygen reduction behavior of RuO<sub>2</sub>/Ti, IrO<sub>2</sub>/Ti and IrM (M: Ru, Mo, W, V) O<sub>x</sub>/Ti binary oxide electrodes in a sulfuric acid solution. *Electrochem. Commun.* **10**, 668–672 (2008).
- Takasu, Y. et al. An examination of the oxygen reduction reaction on RuO<sub>2</sub>-based oxide coatings formed on titanium substrates. *Catal. Today* **146**, 248–252 (2009).
- Nam, K.-D. et al. Partially oxidized niobium carbonitride as a non-platinum catalyst for the reduction of oxygen in acidic medium. *Electrochim. Acta* **55**, 7290–7297 (2010).
- Li, H. et al. Analysis of the limitations in the oxygen reduction activity of transition metal oxide surfaces. *Nat. Catal.* **4**, 463–468 (2021).
- Chan, K. & Nørskov, J. K. Electrochemical barriers made simple. *J. Phys. Chem. Lett.* **6**, 2663–2668 (2015).
- Chan, K. & Nørskov, J. K. Potential dependence of electrochemical barriers from ab Initio calculations. *J. Phys. Chem. Lett.* **7**, 1686–1690 (2016).
- Chen, J.-F. et al. Reversibility iteration method for understanding reaction networks and for solving microkinetics in heterogeneous catalysis. *ACS Catal.* **6**, 7078–7087 (2016).
- Campbell, C. T. Finding the rate-determining step in a mechanism: comparing DeDonder relations with the “degree of rate control”. *J. Catal.* **204**, 520–524 (2001).
- Stegelmann, C., Andreasen, A. & Campbell, C. T. Degree of rate control: how much the energies of intermediates and transition states control rates. *J. Am. Chem. Soc.* **131**, 8077–8082 (2009).

38. Yandulov Dmitry, V. & Schrock Richard, R. Catalytic reduction of dinitrogen to ammonia at a single molybdenum center. *Science* **301**, 76–78 (2003).
39. Zhang, L. et al. A theoretical study of the effect of a non-aqueous proton donor on electrochemical ammonia synthesis. *Phys. Chem. Chem. Phys.* **20**, 4982–4989 (2018).
40. Singh, A. R. et al. Electrochemical ammonia synthesis—the selectivity challenge. *ACS Catal.* **7**, 706–709 (2017).
41. Zhou, F. et al. Electro-synthesis of ammonia from nitrogen at ambient temperature and pressure in ionic liquids. *Energy Environ. Sci.* **10**, 2516–2520 (2017).
42. Kresse, G. & Furthmüller, J. Efficiency of ab-initio total energy calculations for metals and semiconductors using a plane-wave basis set. *Comput. Mater. Sci.* **6**, 15–50 (1996).
43. Kresse, G. & Hafner, J. Ab initio molecular-dynamics simulation of the liquid-metal amorphous-semiconductor transition in germanium. *Phys. Rev. B* **49**, 14251–14269 (1994).
44. Kresse, G. & Furthmüller, J. Efficient iterative schemes for ab initio total-energy calculations using a plane-wave basis set. *Phys. Rev. B* **54**, 11169–11186 (1996).
45. Perdew, J. P., Burke, K. & Ernzerhof, M. Generalized gradient approximation made simple. *Phys. Rev. Lett.* **77**, 3865–3868 (1996).
46. Hammer, B., Hansen, L. B. & Nørskov, J. K. Improved adsorption energetics within density-functional theory using revised Perdew-Burke-Ernzerhof functionals. *Phys. Rev. B* **59**, 7413–7421 (1999).
47. Blöchl, P. E., Jepsen, O. & Andersen, O. K. Improved tetrahedron method for Brillouin-zone integrations. *Phys. Rev. B* **49**, 16223–16233 (1994).
48. Kresse, G. & Joubert, D. From ultrasoft pseudopotentials to the projector augmented-wave method. *Phys. Rev. B* **59**, 1758–1775 (1999).
49. Grimme, S. et al. A consistent and accurate ab initio parametrization of density functional dispersion correction (DFT-D) for the 94 elements H-Pu. *J. Chem. Phys.* **132**, 154104 (2010).
50. Klimeš, J., Bowler, D. R. & Michaelides, A. Van der Waals density functionals applied to solids. *Phys. Rev. B* **83**, 195131 (2011).
51. Cao, X.-M. et al. An understanding of chemoselective hydrogenation on crotonaldehyde over Pt(111) in the free energy landscape: the microkinetics study based on first-principles calculations. *Catal. Today* **165**, 71–79 (2011).
52. Henkelman, G., Uberuaga, B. P. & Jónsson, H. A climbing image nudged elastic band method for finding saddle points and minimum energy paths. *J. Chem. Phys.* **113**, 9901–9904 (2000).
53. Henkelman, G. & Jónsson, H. A dimer method for finding saddle points on high dimensional potential surfaces using only first derivatives. *J. Chem. Phys.* **111**, 7010–7022 (1999).
54. Kästner, J. & Sherwood, P. Superlinearly converging dimer method for transition state search. *J. Chem. Phys.* **128**, 014106 (2008).
55. Methfessel, M. & Paxton, A. T. High-precision sampling for Brillouin-zone integration in metals. *Phys. Rev. B* **40**, 3616–3621 (1989).
56. Pajkossy, T., Wandlowski, T. & Kolb, D. M. Impedance aspects of anion adsorption on gold single crystal electrodes. *J. Electroanal. Chem.* **414**, 209–220 (1996).
57. Pajkossy, T. & Kolb, D. M. Double layer capacitance of Pt(111) single crystal electrodes. *Electrochim. Acta* **46**, 3063–3071 (2001).
58. Trasatti, S. Work Function, electronegativity, and electrochemical behaviour of metals II: potential of zero charge and “electrochemical” work functions. *J. Electroanal. Chem.* **33**, 351–378 (1971).
59. Chen, J. et al. CATKINAS: A large-scale catalytic microkinetic analysis software for mechanism auto-analysis and catalyst screening. *J. Comput. Chem.* **42**, 379–391 (2021).

## Acknowledgements

J.X. acknowledges the financial support from the National Key Research and Development Program of China (no. 2021YFA1500702) (J.X.), the National Natural Science Foundation of China (no. 22172156) (J.X.), the DNL Cooperation Fund, CAS (DNL202003) (J.X.), the AI S&T Program of Yulin Branch, Dalian National Laboratory for Clean Energy, CAS, Grant No. DNL-YL A202205 (J.X.). We also thank Prof. Xuefeng Zhu and Wenhao Zhang for discussions on this topic.

## Author contributions

J.X. conceived and directed the project. H.L. conducted all the calculations and the most of data analyses. J.L. and H.J. contributed to part of the experiments summary and computational analyses, respectively. H.L. wrote the manuscript with contributions from all authors. All authors discussed the results and commented on the manuscript.

## Competing interests

The authors declare no competing interests.

## Additional information

**Supplementary information** The online version contains supplementary material available at <https://doi.org/10.1038/s41467-023-35785-w>.

**Correspondence** and requests for materials should be addressed to Jianping Xiao.

**Peer review information** *Nature Communications* thanks Yuzheng Guo and the other anonymous reviewer(s) for their contribution to the peer review of this work.

**Reprints and permissions information** is available at <http://www.nature.com/reprints>

**Publisher's note** Springer Nature remains neutral with regard to jurisdictional claims in published maps and institutional affiliations.

**Open Access** This article is licensed under a Creative Commons Attribution 4.0 International License, which permits use, sharing, adaptation, distribution and reproduction in any medium or format, as long as you give appropriate credit to the original author(s) and the source, provide a link to the Creative Commons license, and indicate if changes were made. The images or other third party material in this article are included in the article's Creative Commons license, unless indicated otherwise in a credit line to the material. If material is not included in the article's Creative Commons license and your intended use is not permitted by statutory regulation or exceeds the permitted use, you will need to obtain permission directly from the copyright holder. To view a copy of this license, visit <http://creativecommons.org/licenses/by/4.0/>.

© The Author(s) 2023